Received: 17 December 2021 | Revised: 18 March 2022 | Accepted: 24 April 2022

DOI: 10.1002/suco.202100890

ARTICLE

fib CEB-FIP WILEY

Thermo-mechanical experiments on reinforced concrete beams: Assessing thermal, mechanical, and mixed impacts on fiber optic measurements

Felix Clauß | **Mark Alexander Ahrens** | **Peter Mark**

Institute of Concrete Structures, Faculty of Civil and Environmental Engineering, Ruhr University Bochum, Bochum, Germany

Correspondence
Felix Clauß, Institute of Concrete Structures, Faculty of Civil and Environmental Engineering, Ruhr University Bochum, Universitätsstraße 150, 44801 Bochum, Germany.
Email: felix.clauss@rub.de

Funding information
German Research Foundation, Grant/Award Number: 398216472

Abstract

Strain and temperature measurements on reinforced concrete structures with Rayleigh-based fiber optic sensors (FOS) promise dense data networks of crucial structural parameters. In this context, the measurement of temperature and mechanical strain is invariably intertwined, precipitating in a frequency shift recorded via FOS. Consecutive experiments were carried out on reinforced concrete beams under mechanical, thermal, and thermo-mechanical loading. Basic analysis of fiber optics equations indicates the sensitivities toward both influences. These are quantified and juxtaposed in experiments, first separately and subsequently combined. As concerns temperature measurement, the slightest tensile forces exerted onto the FOS may engender distortions of several degrees Celsius. Conversely, strain measurements are affected by temperature changes to a lesser degree. Nevertheless, the level of strain to be sensed and the severity of corrupting temperature shifts must be carefully weighted. The article raises awareness for the coupling of temperature and strain and enables the practitioner to identify and assess perturbations.

KEYWORDS

concrete, experiments, fiber optic sensor, interaction, strain, temperature, thermo-mechanical

1 | INTRODUCTION

As with people, infrastructure is aging. Detecting the signs of the times in our structures as early as possible requires more than a keen eye. There is a wide range of approaches to monitoring structures, subsumed under the concept of structural health monitoring. These range from classical electrical,[1–3] to acoustic,[4,5] to fiber optic methods.[6–8] FOS offer the advantage of measuring strain[9] and temperature[10,11] at a pitch of less than one millimeter and high frequency over a length of tens of meters.[12,13] These advantages have qualified fiber optics not only for practical research[14,15] but also for investigations with basic research underpinnings.[16–18] In addition to applications in civil engineering, this technique is gaining traction in other disciplines such as geotechnics,[19] hydrology,[20] and tunneling.[21] Unlike

Discussion on this paper must be submitted within two months of the print publication. The discussion will then be published in print, along with the authors' closure, if any, approximately nine months after the print publication.

strain measurement, temperatures are rarely measured in applications involving FOS.[22–25]

FOS simultaneously respond to strain and temperature changes. Both effects are coupled. This inherent property, which appears to be an advantage at first glance, implies a challenge in FOS application. Depending on the task, one measured variable, that is, strain or temperature, must be isolated. For temperature measurements, sensors are mechanically decoupled. Residual strain not decoupled, for example, due to friction, may falsify temperature measurement. In contrast to laboratory tests, temperature changes during the diurnal or annual cycle are constitutive elements of practice contexts. This natural temperature change must be recorded and eliminated from analysis in structural applications. To compensate for effects of temperature in strain measurements, an additional fiber—not attached to the material—is commonly employed.

The engineer must deal with such corrupting cross-effects (temperatures in strain measurements and strains in temperature measurements). As mentioned above, one option consists of compensating for them in strain measurements. An alternative course of action lies in quantifying the corrupting temperature shift and, if necessary, estimating and accepting an error. In either case, detailed knowledge of the extent of strain and temperature coupling is required to apply the technique deliberately.

This is where this article comes in. First, necessary explanations of the temperature and strain calculations from the initially measured frequency shift are given. Then, three own experiments (mechanical, thermal, and thermo-mechanical loading of the test specimens) are outlined and evaluated. These experiments usher in the investigation of fiber optics with regards to the specific measurement of the primary influence and the quantification of the respective cross-effect.

As will be presented in the ensuing chapter, the *mechanical* test lays the foundation for this. The temperature influence is comparatively easy to minimize due to control over environmental conditions in the laboratory setting. In the *thermal* test setting, the interaction of temperature and strain can be deduced from the temperature recordings of the FOS. Cross-effects are detected and quantified. Finally, the *thermo-mechanical* test serves to ascertain the corrupting impact of temperature on strain measurements.

2 | FIBER OPTICS

The technological antecedent to the quasi-continuous measurement offered by FOS lies in the distributed measuring technique of fiber Bragg grating (FBG) sensors.[26–29] The fiber's material (the refractive index) is changed at a singular point (Bragg grating) using UV radiation. Consequently, employing measurements of the reflected light's wavelength λ at said point (or its change $\Delta\lambda$), strains $\Delta\varepsilon$ or temperature changes ΔT can be calculated. The strain response (Equation 1) results from both the physical elongation affecting the sensor and the change in refractive index due to photoelastic effects ($[n^2/2]\cdot p_e$). The thermal response results from the inherent thermal expansion of the fiber material (α) and the temperature dependence of the refractive index ($[\mathrm{d}n/\mathrm{d}T]/n$).[27,30,31]

$$\frac{\Delta\lambda}{\lambda}=\left[1-\left(\frac{n^2}{2}\right)\cdot p_{\mathrm{e}}\right]\Delta\varepsilon+\left[\alpha+\frac{\frac{\mathrm{d}n}{\mathrm{d}T}}{n}\right]\Delta T, \tag{1}$$

where $\Delta\lambda$ is the shift in Bragg wavelength (nm); λ is the Bragg wavelength (nm); n is the refractive index; p_e is the photoelastic coefficient; $\Delta\varepsilon$ is the strain change (με); α is the coefficient of thermal expansion; ΔT is the temperature change (°C).

In the quasi-continuous measurement system employed here,[12] that is, FOS, a laser directs light into glass fiber. Microscopic imperfections of the glass caused by melting during its production process lead to slight variations of the refractive index along the fiber.[32,33] The resulting Rayleigh backscatter of the emitted light is measured. The signal contains location-dependent frequencies that rise with increasing distance from the detector (measuring system).[13]

Analogous to the measured wavelength shift in FBG sensors ($\Delta\lambda/\lambda$), with FOS, changes in temperature and strain lead to a frequency shift ($\Delta\nu/\nu$).[13] In most practical cases, the effects of temperature and strain will dominate the spectral response of Rayleigh backscatter.[34,35] Nevertheless, the measurement results are additionally affected—although to a lesser extent—by environmental conditions such as pressure, humidity, and electromagnetic fields.[36] The similarity of FBG and quasi-continuous FOS approaches may be demonstrated in mathematical expressions. When the terms in brackets of Equation 1 (FBG) are transformed into constants and the wavelength (shift) is replaced by the frequency (shift), Equation 2 (FOS) is obtained, which is well known from quasi-continuous metrology:

$$-\frac{\Delta\nu}{\nu}=K_{\varepsilon}\cdot\Delta\varepsilon+K_{\mathrm{T}}\cdot\Delta T, \tag{2}$$

where $\Delta\nu$ is the frequency shift (GHz); ν is the mean optical frequency (GHz); $K_{\mathrm{T}}=6.45\cdot10^{-6}$ is the temperature coefficient (1/°C); $K_{\varepsilon}=0.78\cdot10^{-6}$ is the strain coefficient (1/με).

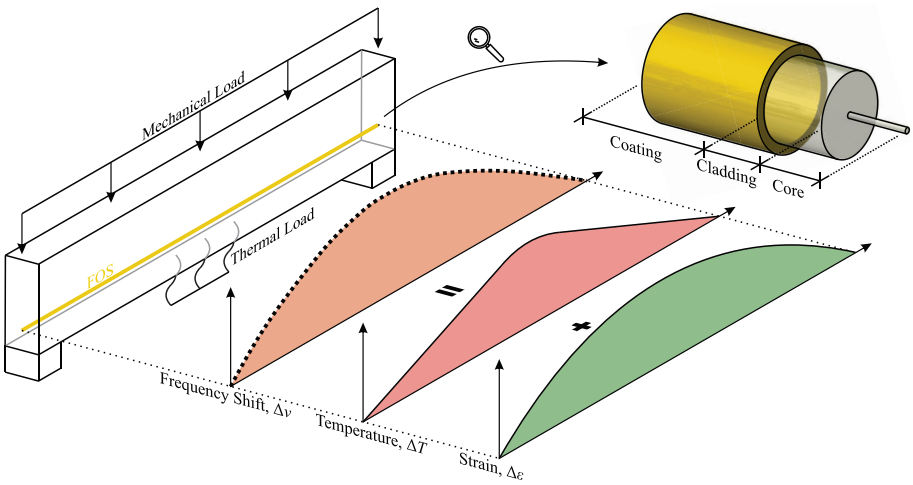

FIGURE 1 Temperature and strain changes induce frequency shift

By mathematical conversion and the introduction of the relationship between the frequency ν, wavelength λ and velocity c, we obtain:

$$\Delta\nu = -\left[\frac{K_T \cdot c}{\lambda}\cdot\Delta T + \frac{K_\varepsilon \cdot c}{\lambda}\cdot\Delta\varepsilon\right] = \frac{1}{k_T}\cdot\Delta T + \frac{1}{k_\varepsilon}\cdot\Delta\varepsilon \quad (3)$$

with $\nu = c/\lambda$, c is the speed of light (m/s) and λ the mean optical wavelength (nm); $k_T = -\lambda/(K_T \cdot c) = -0.638$ the conversion factor (°C/GHz); $k_\varepsilon = -\lambda/(K_\varepsilon \cdot c) = -6.67$ the conversion factor (με/GHz).

Equations 1 and 2 as well as Figure 1 illustrate the duality, that is, the coupling of the influences—changes in strain and temperature. The effect of both influences considered (a) separately and (b) in combination leads to a change in frequency shift. A comparison of conversion factors elucidates to the different weighting of the two influences with respect to the frequency shift. Their coupling means that as soon as temperature and strain influences are present simultaneously, additional steps for making inferences as to each individual factor are rendered necessary.

In this vein, available mathematical approaches are suggested in previous studies.[31,37] A convenient solution is the separate isolated measurement of temperatures using an additional fiber. For strain measurement, the FOS is mechanically coupled to the desired component (usually by bonding). In addition to mechanical strain, this sensor simultaneously measures elongation due to temperature (mixing effects). A second sensor, which does not pick up any strain due to its freely movable position in a tube, ideally solely measures temperature-related frequency shifts. The latter result is finally subtracted from the mixed frequency shift. The result is a temperature-compensated strain measurement.

The right part of Equation 3 can be transformed to calculate strain (Equation 4) or temperature (Equation 5). Usually, it is assumed that the respective other influence has ideally been excluded and is therefore equal to 0. However, the rear term of Equations 4 and 5 can quantify how far the target measurand is influenced by the respective other quantities (cross-effect).

An indication of this is provided by the ratio k_ε/k_T or k_T/k_ε. In Sections 4.3 and 4.4 this cross-effect in the measurements will be discussed in more detail.

$$\Delta\varepsilon = k_\varepsilon \cdot \Delta\nu - \frac{k_\varepsilon}{k_T}\cdot\Delta T, \quad (4)$$

where $\frac{k_\varepsilon}{k_T} \approx 10$ (με/°C).

$$\Delta T = k_T \cdot \Delta\nu - \frac{k_T}{k_\varepsilon}\cdot\Delta\varepsilon, \quad (5)$$

where $\frac{k_T}{k_\varepsilon} \approx \frac{1}{10}$ (°C/με).

Equation 5, in principle, emphasizes a linear dependence of the temperature on the frequency shift scaled with the factor k_T. In previous studies,[34,35] however, a fourth order polynomial approach according to Equation 6 is recommended for temperature measurements. Since the relationship between the frequency shift and temperature must be established individually in each application, an accompanying temperature measurement is necessary. Linear regression is then used to find the coefficients β_0 to β_4 that best represent the model of temperature change in a least-squares fashion. β_0 represents the ambient temperature, while the regression coefficient of the linear term adapts the general manufacturer's data concerning K_ε to the local conditions. Lastly, the remaining coefficients capture potential higher-order components.

$$\Delta T = \beta_0 + \beta_1 \cdot \Delta\nu + \beta_2 \cdot \Delta\nu^2 + \beta_3 \cdot \Delta\nu^3 + \beta_4 \cdot \Delta\nu^4. \quad (6)$$

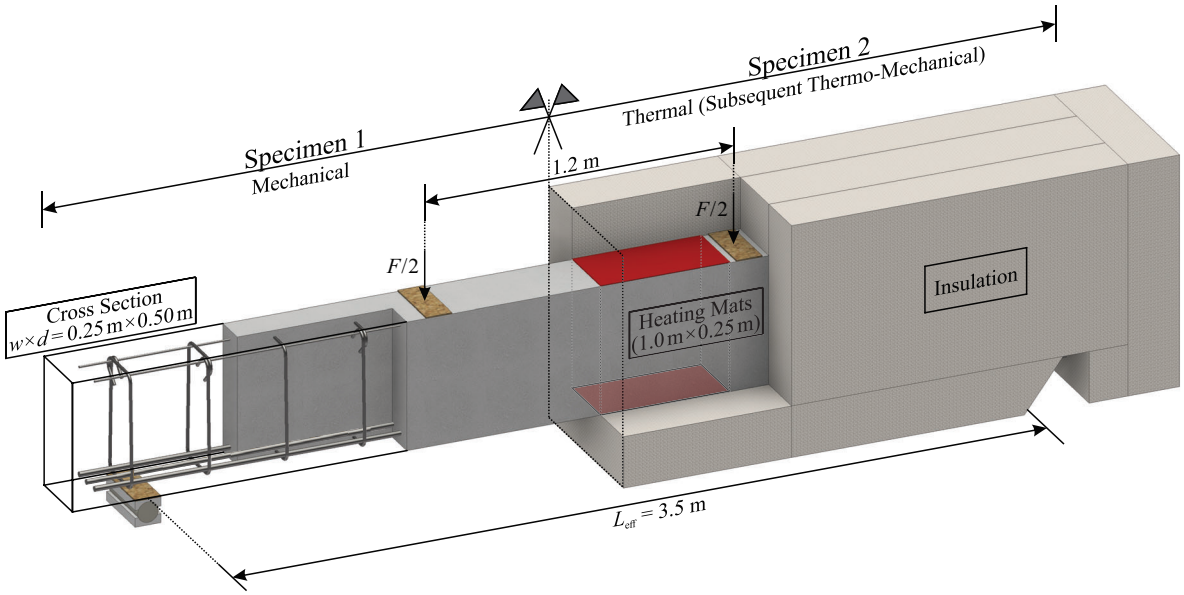

FIGURE 2 Test specimens for the mechanical, thermal, and thermo-mechanical tests

3 | EXPERIMENTS

3.1 | Specimens

The objective is to investigate fiber optic measurement technology subjected to coupled thermo-mechanical influences. Following the principle of one-factor-at-a-time (OFAT), the effects on the test specimen—mechanical and thermal—are initially examined individually and later in combination. Hence, a total of three tests were performed on two test specimens. In contrast to the mechanical test conducted with the first test specimen, the thermal test on the second one is non-destructive. This allows for an additional experiment to be carried out on the same sample body. A mechanical load follows the initial purely thermal test once a thermal steady state is reached—the thermo-mechanical test results from the loading in the heated state.

Two reinforced concrete (RC) beams with identical external dimensions ($w \times d \times L = 0.25 \times 0.50 \times 3.9$ [m]) and reinforcement layout (flexural reinforcement 3Ø20 mm [9.42 cm^2], structural reinforcement 2Ø8 mm [1.01 cm^2] and stirrups Ø12 mm/30 cm [7.54 cm^2/m]) are fabricated. In the mechanical as well as in the later thermo-mechanical test, the specimens (see Figure 2) are loaded by two concentrated loads under four-point bending. With a span of $L_{\text{eff}} = 3.5$ m and a distance between the concentrated loads of 1.2 m, a constant bending moment is generated in the area between.

In analogy to this constant load, the second test specimen is heated to approximately 40°C in its middle section on both the upper and lower side. The heat is induced via two heating mats[38] with a length of 1.0 m and a width of 0.25 m (see Figure 2, marked in red). In a previous study,[39] among other methods, this technique for temperature induction was investigated: the low weight but especially their high flexibility regarding deformations qualifies the heating mats for this application. In order to separate the test specimen to be heated from the colder outside air, it was completely encased in polystyrene of 20 cm thickness. Merely the locations of support and later load application were omitted and designed in such manner that deformation and rotation at the supports during loading is rendered possible in unhindered fashion.

3.2 | Sensor placement and installation

3.2.1 | Placement

Throughout the experiments, the targeted quantities, that is, strain and temperature, are recorded. Strain gauges and FOS were used to record strain, and thermocouples (TC) and FOS were used to record temperature. Figure 3 shows the consistent sensor placement for the experiments.

During mechanical testing, FOS1 and 2 measure the concrete strains along a lateral surface. Here, they are glued on. Expecting a linear strain profile over the depth of the specimen due to the (constant) bending moment, the FOS were placed in the direction of the beam's longitudinal axis and staggered over its depth. The loops result in nine layers (e.g., FOS1 and 2 in Figure 3). Strain

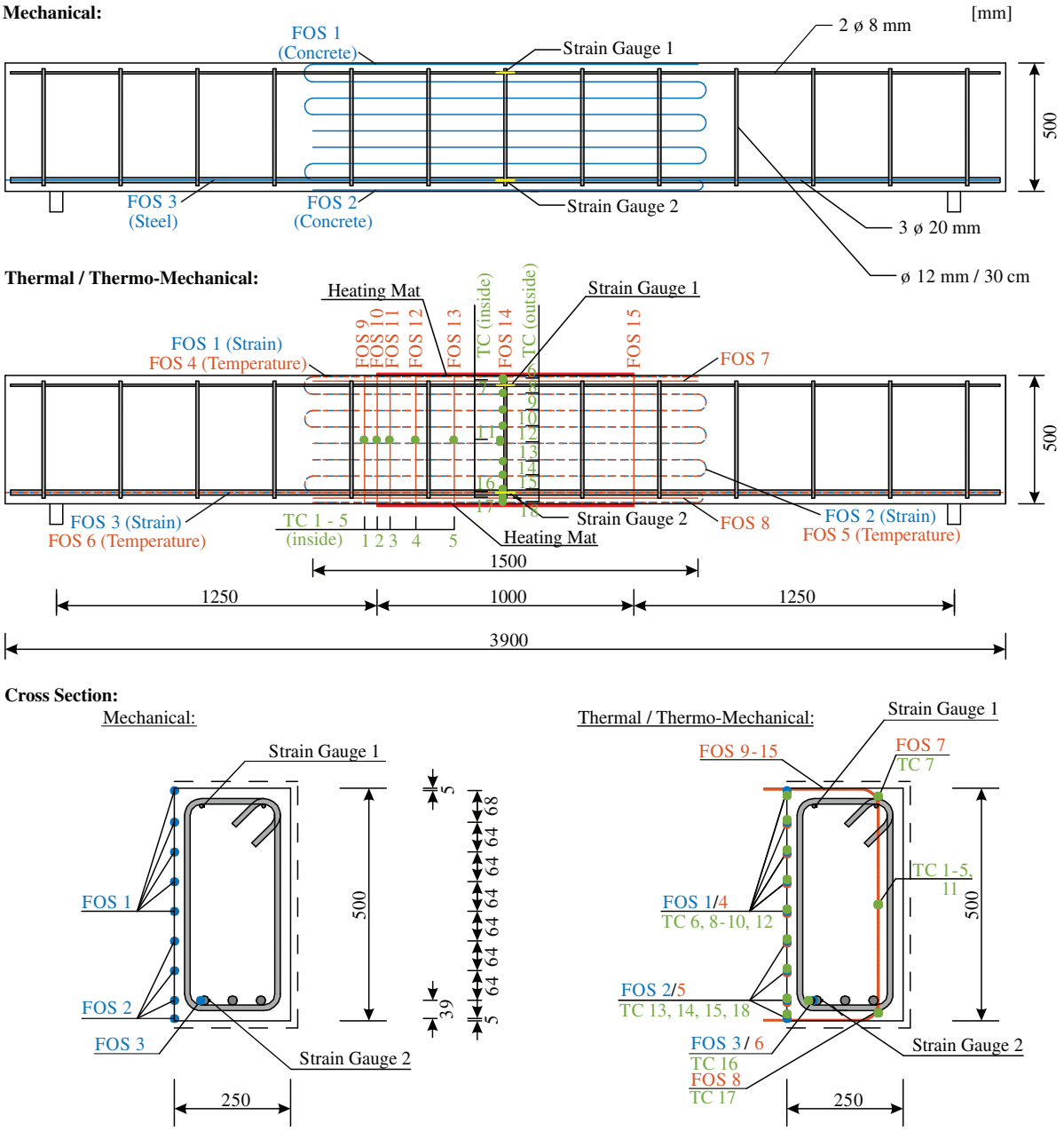

FIGURE 3 Geometry, reinforcement, and sensor layout

measurements varies significantly along the body's *length* due to concrete cracking and are therefore recorded in finely grained millimeter range intervals (0.65 mm spacing of the measuring points). Conversely, strain measurements along the body's *depth* (e.g., FOS1 and 2) vary less intensely, allowing for a coarser gradation and more space between measuring points. Finally, FOS3 measures the strain of the reinforcing steel. For reference, strain gauges were attached to the reinforcing steel (top and bottom) in the middle section of the specimen.

In order to only record the temperatures in the *thermal* test, FOS7 and 8 were placed horizontally and FOS9 to 15 vertically in the specimen. These FOS are guided through plastic capillaries inside the specimen as to avoid tensile forces. Their insertion is oriented along the points at which the largest temperature changes in the beam are to be expected.

Since the optical fibers always detect strain and temperature changes simultaneously, measuring strain requires quantifying the corrupting cross-effect exerted by temperature shifts. Hence, installing a separate fiber recording temperature only allows for temperature compensation. Said FOS is placed directly next to the fiber for strain measurement. Parallel to FOS1 to 3 for the strain measurement from the mechanical test, the capillary-guided FOS4 to 6 (capillary diameter approximately

TABLE 1 Objectives of the individual FOS

Test	FOS strain	FOS for temperature compensation	FOS temperature	TC temperature
Mechanical	1			
	2			
	3			
Thermal			7	7
			8	17
			9	1
			10	2
			11	3
			12	4
			13	5
			14	11
			15	
+ Mechanical	1	4		6/8/9/10/12
	2	5		13/14/15/18
	3	6		16

1.5 mm) are added in the thermo-mechanical test. They can be used to compensate for the corrupting temperature cross-effects in the strain measurement values (cf. Section 2).

In addition to the 15 FOS, 18 thermocouples are installed. Except for the looped FOS4 and 6, they are always located in the center of the sensor. For these two, however, one thermocouple is placed in the center of each layer. Table 1 links the individual FOS and TC and assigns their numbering to the experiments.

Beyond the fiber optics and conventional measurement techniques (strain gauges and thermocouples), the speckle pattern for digital image correlation (DIC) is added to the opposite lateral surface (opposite to the surface shown in Figure 3). Although the results of this measurement technique are not part of the following analysis, their collection nevertheless influences the experimental procedure. The load increase must be gradual. At each level, the test is stopped, the insulation is opened, a photo is taken and the insulation is closed again.

3.2.2 | Installation

The FOS must be firmly bonded to the concrete component for strain measurement. As described in an earlier study,[39] the Polytec PT AC2411 adhesive is suitable for this purpose. Relevant work accounting for strain transfer mechanism from the base material (e.g., concrete) to FOS can be found in previous studies.[40–42]

First, a longitudinal groove is milled into the rebars. Afterward, the FOS is bonded into this groove. The FOS leaves this groove at each end of the rebar and is guided out of the formwork. These areas (from the point where it leaves the rebar until it is completely guided out of the formwork) are protected by plastic capillaries. The fibers coming out of the formwork then lead into tubes outside the formwork and are thus protected (see Figure 4, left). After curing, FOS1 and 2 are bonded to the surface of the concrete specimen in loops as described in a previous study[43] and depicted in Figure 3 to record the strain field.

To measure temperatures with FOS, they are either installed in plastic capillaries and (a) glued on or (b) embedded directly in concrete (see Figure 4, right). The FOS remain freely movable within the capillaries when installed (e.g., after concreting). Employing this technique, encapsulating and thereby protecting the FOS tasked with only measuring temperature, strain transfer from the component into the fiber, which would here constitute a corrupting cross-effect, is avoided. For referencing and later calibration (see Section 4.3) of the temperature measurements of the FOS, thermocouples (see Figure 4, right) are attached to the capillaries.

3.3 | Test setup and experimental procedure

The test specimens are loaded externally by four-point bending. As shown in Figure 5, a load induction traverse spreads the force of the servo-hydraulic cylinder evenly

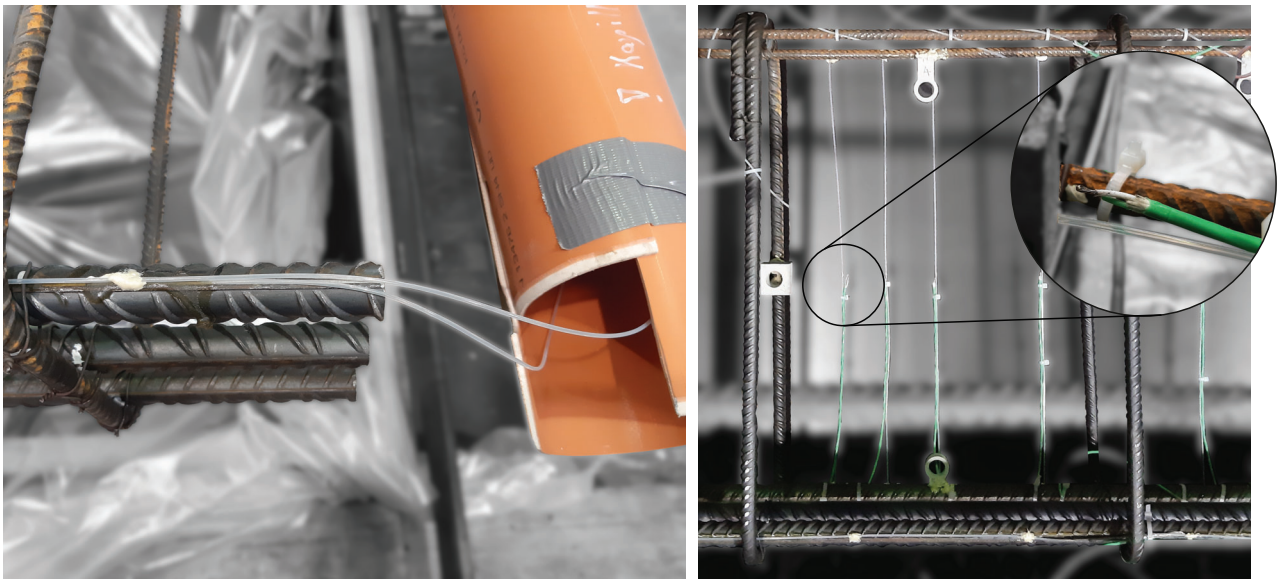

FIGURE 4 Left: Protection of the FOS in capillaries and pipes for concreting. Right: Mounting of the FOS and thermocouples

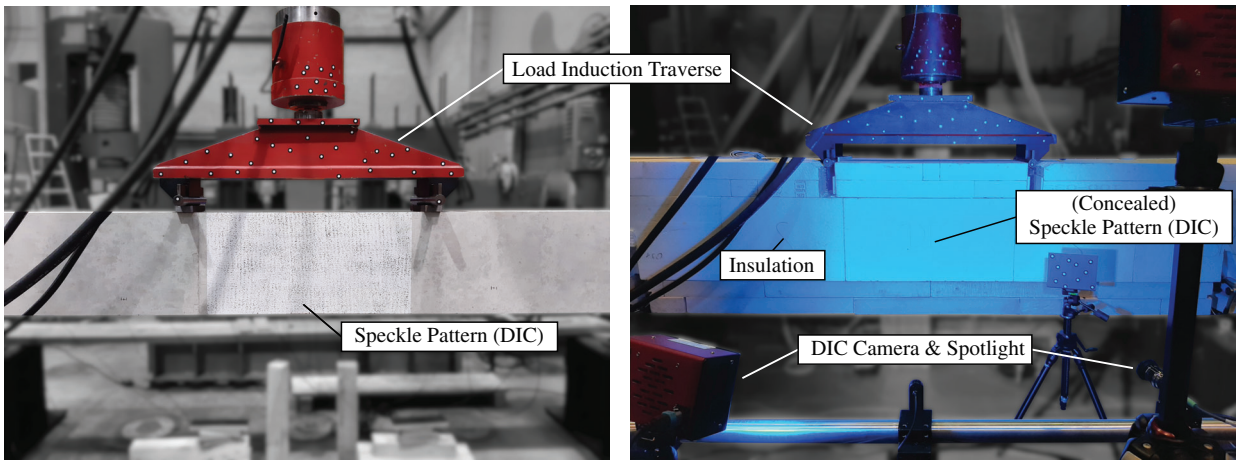

FIGURE 5 Setup of the mechanical (left) and the thermo-mechanical (thermal) test (right)

over the two load application points. DIC measurements are carried out in conjunction with the fiber optical and conventional measurements. The thermo-mechanical test requires a gradual increase in load and interruption at regular intervals to remove the insulation in front of the speckle pattern. Following the capture of the photos, the insulation is closed again, the load is further increased, and the process is repeated. On the other hand, in the mechanical test, the DIC measurement takes place continuously with a permanently unobstructed view as no insulation is required.

The first test specimen is subjected to load-controlled force (0.5 kN/s) in the mechanical test, increasing across gradual 5 kN steps initially until 100 kN is reached, and ensuingly 10 kN steps until reinforcement yielding occurs at a load of approximately 330 kN. The second test specimen is subjected to 40 °C in the thermal test on the top and bottom sides (see Figure 2). This temperature is maintained for 7 days (168 h) until a thermal steady state is reached in the interior. Subsequently, the test specimen is subjected to a stepwise loading procedure identical to the purely mechanical test.

3.4 | General results

FOS1 and 2 are attached in loops to the lateral surface of the first test specimen (mechanical test). Only the longitudinal sections of these FOS are considered in the evaluations. In accordance with Figure 3, there are nine layers

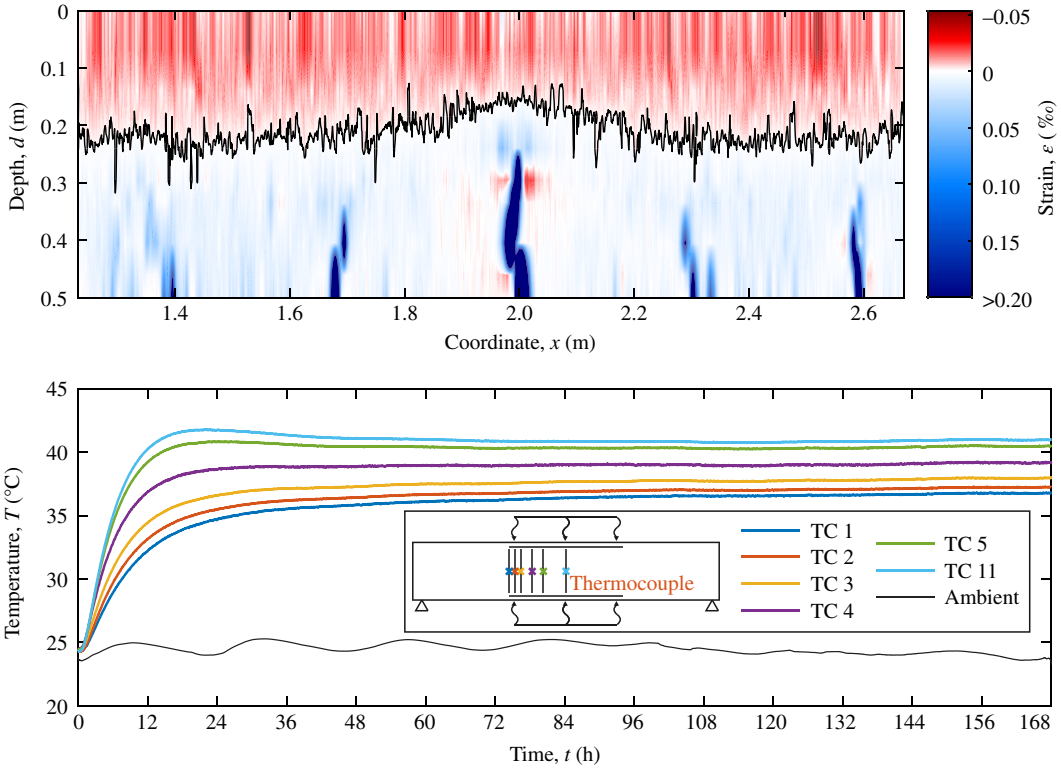

FIGURE 6 Top: Strain field derived from the nine levels of FOS1 and 2 for a load of $F = 35$ kN. Bottom: Temperature development in the thermal test

along the depth. In these nine sections, a strain measurement is recorded every 0.65 mm of the fiber. Consequently, measured values are obtained on nine levels of the specimen, every 0.65 mm. These measured values can be processed as a two-dimensional strain field, as shown in Figure 6 on the top. In order to display the strain field over the entire depth (0.5 m), the boundary values are extrapolated (from the uppermost or lowermost level, extrapolation length: 5 mm).

The red regions represent the compressive zone and the light blue ones the tensile zone of the beam under applied loading. Dark blue areas indicate cracks. A black line delimits the compressive zone. This represents the zero crossing between compressive and tensile strains over the depth. Due to the coordinate system starting at the top of the bar (depth [d] increases toward the bottom), the black line simultaneously indicates the compressive zone height.

It is evident that compressive strains (or stresses) occur at the top and tensile strains at the bottom, corresponding to the positive bending moment. As expected, the cracks (dark blue) form in the tensile zone. They form in regular intervals of about 30 cm and grow or propagate from bottom to top. The largest crack in the center at about 2.0 m already slightly reduces the compression zone height. This can be seen by the smaller red region in the vicinity and the black line moving upward in Figure 6.

It should be noted that the width of the dark blue area does not indicate the crack widths. The relative displacement of the crack edges (originating from zero in the uncracked state) locally leads to high strains, which are also carried into neighboring parts due to a certain softness of the adhesive of the FOS. Further details can be found in earlier studies.[44,45]

The lower section of Figure 6 exhibits the measured temperatures of the TC1 to 5 and 11, as well as the ambient temperature. It is to be pointed out that the heating has taken place over 168 h. In the first 12 h, the temperature measured at all TC locations increases sharply. From about 36–48 h, on the other hand, hardly any temperature change can be seen. The small fluctuations in the ambient temperature obviously do not affect the component temperature.

Comparison of the thermocouples indicates that the highest temperature is consistently measured in the center of the test specimen (TC11). The measured temperatures decrease toward the beam's longitudinal end faces, where most temperature loss occurs. Toward both end faces, the influence of the nontempered areas increases.

Overall, the curves (Figure 6 bottom) run affine to each other and consolidate at a constant level after 36–

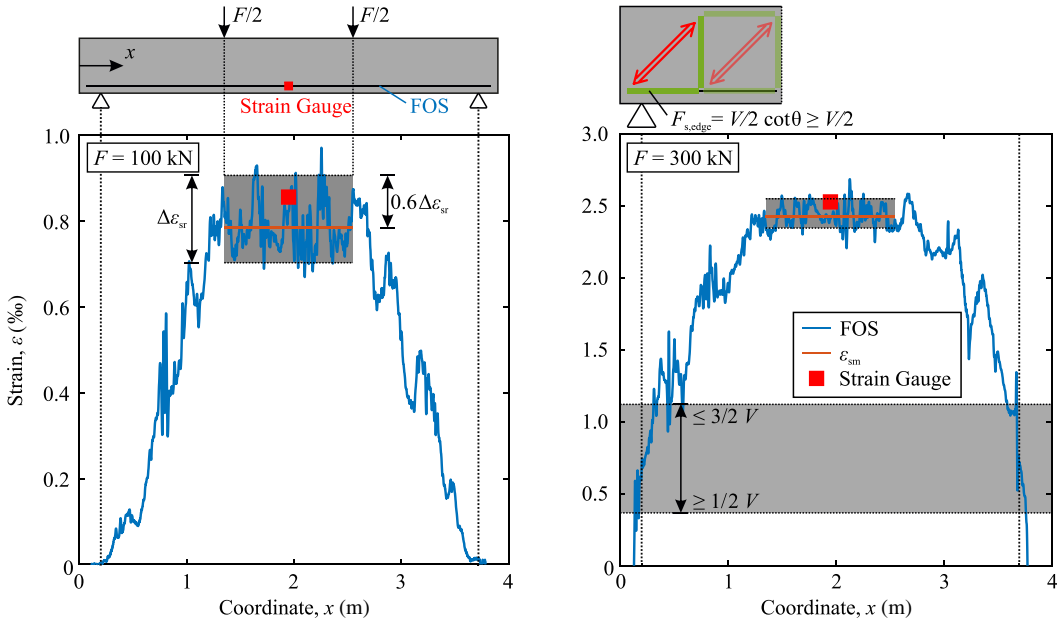

FIGURE 7 Strain measurement with FOS on the reinforcement for 100 kN (left) and 300 kN (right)

48 h. After 168 h, the load increase occurs as part of the *thermo-mechanical* test.

4 | INDIVIDUAL IMPACTS AND INTERACTION

4.1 | Preface to the discussion

Parallel to the mechanical, thermal, and thermo-mechanical tests (themselves), a discussion of said scenarios is presented separately in the ensuing subchapters. In the laboratory, purely mechanical testing against unintended temperature changes is easier to achieve than vice versa. Not only do controlled environmental conditions (e.g., solar radiation or air temperature) limit its influence but also the inertia of thermal conduction of concrete contributes to it. However, solely measuring *strain* as an isolated quantity is a physical impossibility in real-life scenarios. Temperature changes are inherent to the diurnal cycle. Therefore, the explanations first address mechanical strains only and then transition to isolated temperature measurement with FOS. The interaction of targeted measurand and corrupting cross-effects in the thermal test are then analyzed. As a synthesis of said two preceding experiments, the concluding thermo-mechanical test comprises both temperature and strain, as well as their interaction. It provides information about the accuracy of strain measurements under the influence of temperature and enables a discussion of real application scenarios for FOS.

4.2 | Mechanical load

Figure 7 depicts the strain curves of the reinforcement under a load of 100 kN (left) and 300 kN (right). In both diagrams, the strain curve increases from the supports (end faces) to the center and displays some distinct peaks. In the load area between $x = 1.35$ m and 2.55 m, a plateau is formed despite further peaks. Each peak (local increase in strain in the reinforcement) indicates a crack in the concrete at this point. Here, the reinforcement has to absorb the force released by the cracking concrete. As a result, the strain increases locally by leaps and bounds.

For deformation computations of RC members in the cracked state, the average steel strain ε_{sm} [46,47] can be formally calculated using the course of the reinforcing steel strain according to Equation 7.

$$\varepsilon_{sm} = \frac{1}{l_T} \int_0^{l_T} \varepsilon_s(x)\, \mathrm{d}x, \tag{7}$$

where l_T is the transfer length of the released force from the reinforcement into the concrete and $\varepsilon_s(x)$ is the steel strain.

It is obtained by integrating the strain curve in the affected area and is related to its length. Consequently, it idealizes this area via its average value as a constant. This is shown in Figure 7 (left and right) based on the fiber optic measurements between the concentrated loads ($x = 1.35$–2.55 m), that is, the area of constant bending moment.

Furthermore, the strain increment in the reinforcement $\Delta\varepsilon_{sr}$ during cracking can be formally calculated according to Equation 8. It links the average steel strain, the strain in the crack as well as the strain increment.

$$\varepsilon_{sm} = \varepsilon_{s2} - \beta_t \cdot \Delta\varepsilon_{sr}, \tag{8}$$

where ε_{s2} is the steel strain at the location of a crack.

β_t is derived from the bond relationship between the reinforcement and the concrete and can be assumed to be 0.6 for short-term exposure to load.[47] If the average strain is thus raised or lowered, the maximum and minimum strain levels of the reinforcing steel shown in Figure 7 are obtained. The juxtaposition of both load levels depicted in Figure 7, underlines how the maximum and minimum levels are compatible with the measured strains. This finding offers the conjecture that concrete cracking in detail (e.g., tension stiffening[48]) can be further investigated using the fiber optic technique. Promising investigations can be found in previous studies.[17,49,50]

The local strains detected by the strain gauges in the center of the reinforcement also coincide well with the curves of both loads (100 and 300 kN).

In addition, the right of Figure 7 shows that the strain at the supports (dashed line) does not decrease to 0. In cracked RC beams, a truss-like load-bearing behavior develops. In equilibrium, the applied force is transferred to the support by concrete compressive and steel tensile struts (the reinforcement). This results in a constant base level of strain at the support following,[51] even if the corresponding bending moment at this location is equal to 0. Emanating from equilibrium considerations, it is to be deduced that the tensile force at said point always falls between:

$$\frac{V}{2} \cdot \cot\theta \geq F_{s,\text{edge}} \geq \frac{V}{2}. \tag{9}$$

With the general restrictive range of compressive struts' inclination at approximately 18°–45°, the edge tensile force must settle between $3/2\,V$ and $1/2\,V$. Transformed into strain, these limits are plotted in Figure 7 on the right. The comparison again underlines that the measured values fall within the calculated edge tensile force limits.

4.3 | Thermal load

Figure 8 plots the temperature curves measured by FOS and TC at all eight measuring points over the full test duration of 168 h. The measuring points are the locations where the TC are attached to the corresponding FOS

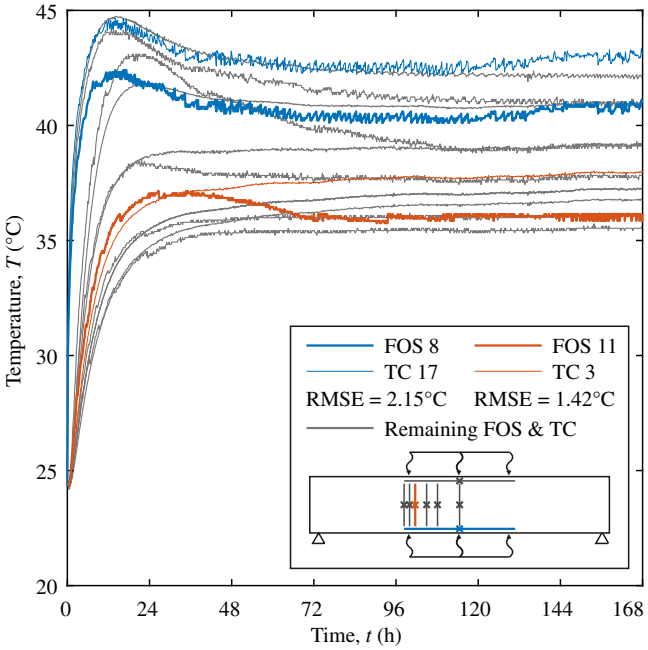

FIGURE 8 Temperature–time courses of FOS 8 and 11 paired with thermocouples 17 and 3

(cf. Figure 3 and Figure 4). To reiterate statements made earlier, all FOS only tasked with temperature measurement are guided in capillary fashion in plastic tubes, thereby avoiding contact between fiber and concrete. Two selected pairs of curves without (FOS8/TC17) and with (FOS11/TC3) influence of moisture changes are highlighted in color. Especially the temperature curves of FOS8 and TC17 display affinity to each other. Nevertheless, an almost constant absolute temperature difference of approximately 2.5 °C can be observed.

For practical application, such offset must be eliminated. For this purpose, a scaling coefficient, that is, conversion factor, adjusts the functional relationship between the temperature change T and the actual measured variable frequency shift $\Delta\nu$ according to Equation 5 or Equation 6.

In practice, such implies that the factor k_T offered by the general specifications of the fiber manufacturer (default) must be calibrated and specified for each individual test to produce accurate temperature measurements.

Mathematically, such is undertaken by linear regression,[52] either simplified using the linear approach according to Equation 5, or employing the fourth order polynomial approach according to Equation 6. The latter offers greater flexibility and a more precise conversion. The computational power required for said regression is easily covered by modern tools. Therefore, said approach is used exclusively in the following.

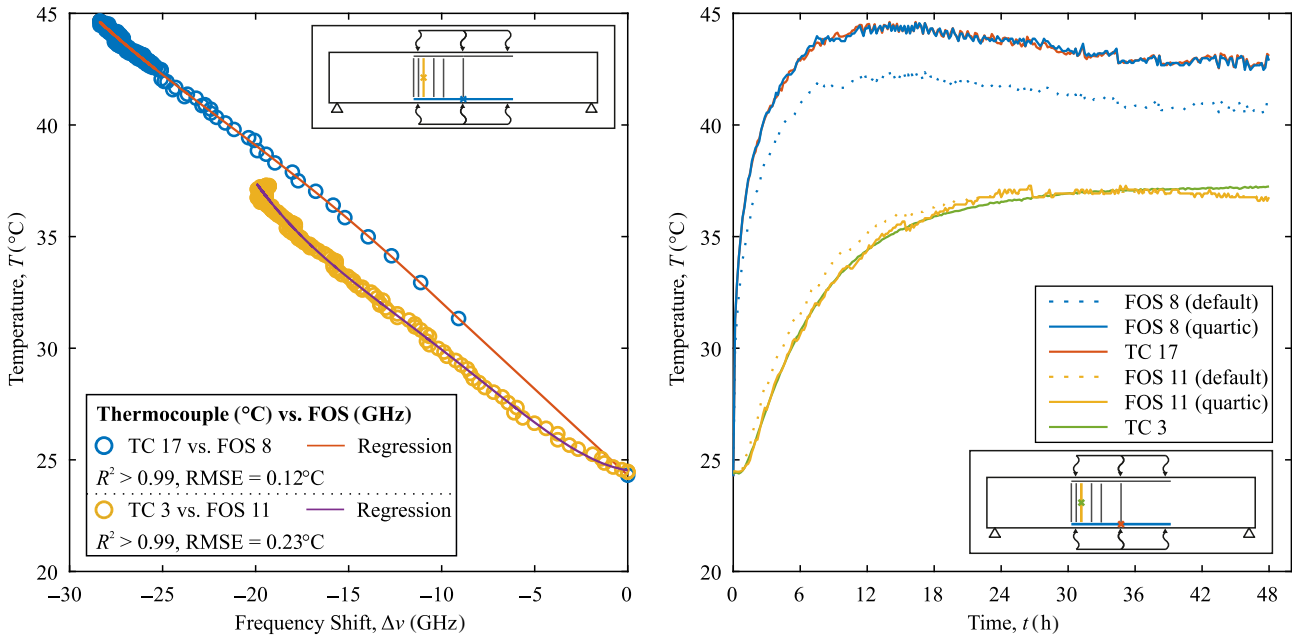

FIGURE 9 Temperature–time courses after regression of the frequency shifts to the actual temperatures

Contrary to the pairing of FOS8 and TC17, a comparison of the trajectories of FOS11 and TC3 uncovers lesser degrees of similarity. Initially, both courses of temperature measurements are close to each other. However, in the time span between 36 and 84 h, they diverge. Finally, beginning approximately at 84 h, they again show a quasi-constant offset of 1.5 °C from one another.

While the unadulterated, more precise measurement temperature in TC3 follows a constant after about 36 h, FOS11 exhibits temperature changes during this period. Hence, fiber optic measurement must be influenced by another effect here. Said effect may reside in what may be coined *parasitic* strains, which stem from friction, for example, an overly narrow bending radius, between FOS and plastic tube. However, differences in humidity or transverse pressure from compression are also known to influence, albeit to a lesser degree, the frequency shift.[34–36] The aging of the coating also exerts potential influence. In order to be able to exclude time-dependent reasons, the regression was therefore limited to the first 48 h during which the deviations are consistently small. The calibration here is thus adapted for a short-term measurement scenario. If a long-term observation, for example, while monitoring, is to be carried out, the exact influences corrupting must be accounted for to ensure.

The left section of Figure 9 depicts the regression of the data measured with TC and the frequency offset of the FOS utilizing the fourth order polynomial approach. Measures of determination close to 1 and low RMSE (root mean square error) prove the high quality of the conversion. In both cases, the graphs follow a quasi-straight progression. The somewhat clearer curvature of TC3 and FOS11 demonstrates that a higher-order approach produces small gains in accuracy here.

The regression is performed for each fiber and the corresponding thermocouple. If the temperatures deduced from FOS frequency shift measurements are computed employing a conversion based on said new relationships, the temperature–time courses on the right of Figure 9. Resultingly, temperature measurements produced by respective TC and FOS pairings are almost congruent.

By means of an example, the temperature measurements produced by FOS7 and 8 along the test specimen's central section are illustrated in Figure 10. Hence, FOS 7 and 8 (length of 1.20 m) extend 10 cm past the central section covered by the heating mat (length of 1 m). This is to ensure temperature detection for the entire heated segment.

After 2 h of heat exposure, areas of decreasing temperature appear toward the edges, resulting from the unavoidable heat loss into the nontempered edge segments of the beam. While the course of FOS8 already appears symmetrical to the center and suggests a plateau, the course of FOS7 shows substantial deviations, especially on the left side. Moreover, less pronounced local deviations are evident on the right side. Due to the constant temperature field with uniform heating of the upper and lower side of the beam via the heating mat, the course of measurements produced by said fibers would a priori be expected to proceed in a congruent fashion. Said expectation is fulfilled when regarding the produced

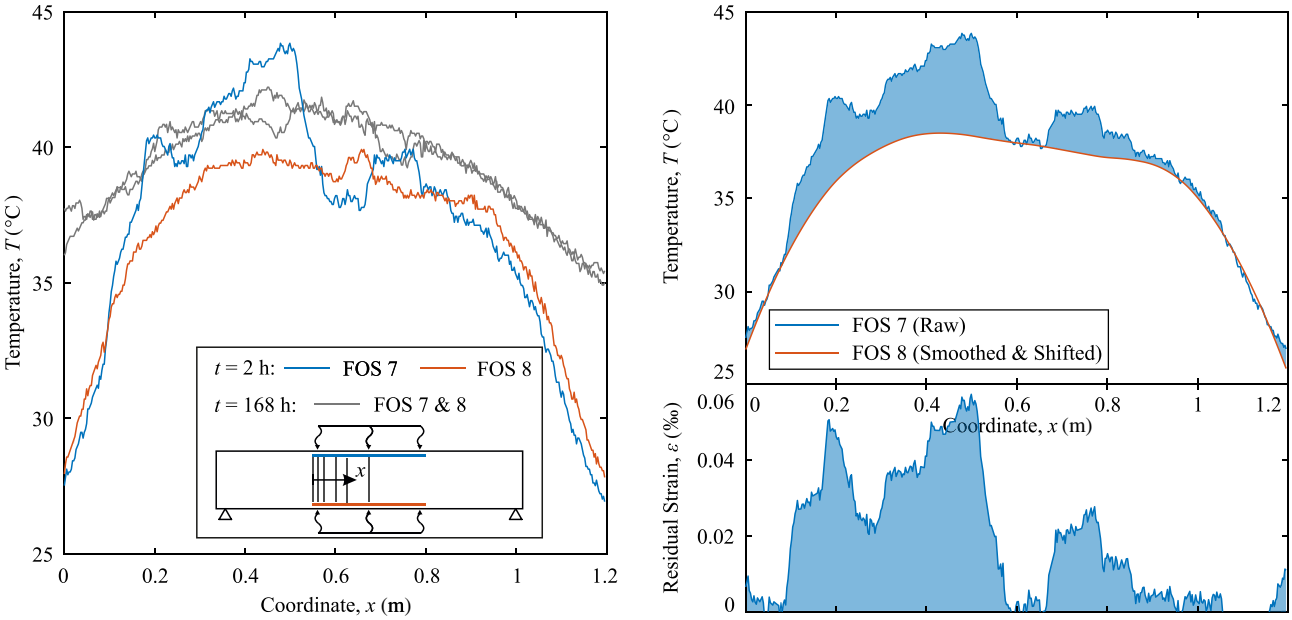

FIGURE 10 Left: Strain affected temperature readings of FOS7 and 8. Right: Residual strains in FOS7 impair temperature readings

measurement curves of FOS7 and 8 after 168 h of test duration (in the background, gray). However, since short-term measurements are prioritized here, it is necessary to discuss the reasons for potential deviations, to quantify their magnitude to be able to estimate the magnitude of error in the measurement.

Since the plot of FOS8 after 2 h is largely as expected, it is the reference of an error estimate in Figure 10, right. For this purpose, it was first smoothed by robust linear regression, which fits each section of 160 measured values with a second order polynomial and reduces the inherent measurement scatter. It was then shifted in the axis of symmetry to the center of the field and brought into agreement with the course of FOS7. This ensures that only local residuals remain and global deviations, for example, due to nonuniform heating of the top and bottom surfaces throughout the measurement range, are eliminated. In Figure 10, bottom right, this residual was finally transformed into strain using the known relationships via the frequency shift and projected onto the gauge length.

This residual strain is interpreted as a parasitic strain, which is not due to temperature influences. Rather, its origin is assumed to be unplanned influences such as friction between the FOS and the capillaries, bending radii that are too tight, or strain induced by deformations of the component. In the case of friction, they can build up over time and also degrade, for example, due to post-slip. It would be wrong to interpret the size of the residual strain as temperature. The maximum value is 0.06 ‰ at the point $x = 0.5$ m, which corresponds to the temperature deviation of 6°C in the diagram above.

To improve the classification of the magnitude, the residual strain can be converted further into a force acting on the fiber. If, for the sake of simplicity, the polyimide coating ($E = 2{,}400$ N/mm^2), which is significantly softer than the core and cladding (silicate glass: $E = 73{,}000$ N/mm^2), is according to previous studies[30,53] neglected, force of only 0.05 N results employing a fiber diameter of 0.125 mm. This corresponds to a weight of approximately 5 g. Even said minimal force leads to an error of approximately 6 °C, consequently, larger forces to correspondingly larger errors.

4.4 | Combined thermo-mechanical load

In principle, thermo-mechanical tests can be carried out in two ways. On the one hand, actions are applied one after the other, as in this case. First, the influence of temperature and afterwards of mechanical load on the measurement can be examined. On the other hand, in terms of real-world application, the second possibility of a contemporary mixed load, as is usually the case on structures (e.g., traffic load and change of temperature in the diurnal cycle) is more representative. It presupposes that the effect of all influences and, if necessary, their interaction is known in advance to ensure a clear assignment of cause and effect. Otherwise, false conclusions might be drawn. The temperature error caused by even small parasitic strains was shown earlier.

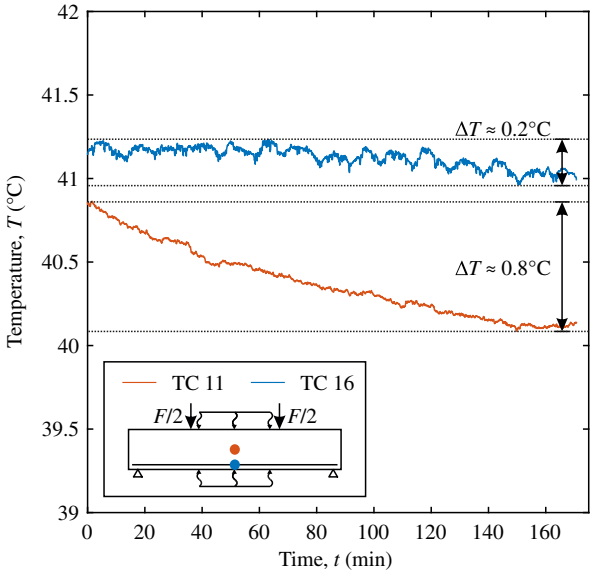

FIGURE 11 Development of temperature over time in the thermo-mechanical test

TABLE 2 Strain error due to temperature change

Residual temperature (°C)	Strain error (‰)
0.8	0.008
5 (winter)	0.05
12 (summer)	0.12

Considering the inverse scenario, temperature errors are to be transformed into equivalent strain errors and evaluated. The central question remains, which findings result from this for the measurement practice.

For the DIC measurements, the load had to be increased stepwise in the thermo-mechanical test. The insulation was briefly removed at each load level on one side, a photo was taken, and the insulation was closed again. The effect of the repeated opening is revealed by the temperatures in Figure 11. Both TC11 and TC16 are located in the middle of the beam, TC11 in the center, TC16 at the edge in close proximity to the heating mats. The temperature in the interior is more affected by the multiple openings than near the edge. In the center (TC11), a temperature difference of 0.8 °C accumulates. The reason for the smaller influence of the thermocouples near the edge, is the continuous heat flux from the nearby heating mats. At the edge, the proximity to the heating mat results in only 0.2 °C.

To assess nonconsideration of such temperature changes on strain measurements with FOS, the temperature changes were transformed from frequency shifts into strains via the known conversions. In Table 2, in addition to the maximum temperature drop due to the opening of the insulation of 0.8 °C, representative temperature differences in the diurnal cycle at structures in summer and winter are given for comparison purposes. The resulting strain error is small in all cases, which explains why strain measurements with FOS are practically much more common than temperature measurements. Their error potential due to mutual influence is much smaller.

Before the start of the load increase, the strain measurement in the test was zeroed. Consequently, purely mechanically induced strains were measured in isolation. Previous temperature changes (in the thermal test), therefore, no longer play a role. Figure 12 shows such a strain measurement of the FOS3 on the longitudinal reinforcement as a white line along the entire beam length. The strain errors listed in Table 2 are plotted as scatter bands around this line. The narrow white band indicates the scatter of the measurement due to the opening-based temperature change, the other gray bands those due to not taking into account hypothetical temperature changes in winter and summer, respectively. Even the more severe summer case ultimately affects the strain measurement only slightly.

For classification, this temperature-related strain scatter can first be compared with the measurement system's (Luna ODiSI 6108) accuracy specifications and the selected measurement mode (High Resolution, Gage pitch 0.65 mm) according to the manufacturer's specifications.[12] A total scatter of 0.047 ‰ is obtained from the sum of accuracy (±0.025 ‰) and repeatability (±0.022 ‰). This but also the absolute magnitude of the strain to be recorded is to be used for the evaluation.

A temperature-related deviation in strain of 0.008 ‰ (0.8 °C) accounts for only 20 % of the total uncertainty of the measurement system. At 5 °C unintended temperature change, the scatter is about as large as the total scatter of the measurement system, at 12 °C more than twice as large (see Table 3). In the worst case, errors from both scatter add up, the total scatter of the measuring system and from unintended temperature deviation, which in turn must be taken into account when determining the acceptable scatter size of the measurement.

In addition to the relative consideration, the absolute magnitude of the strain to be measured also determines whether such scatter plays a role or is negligible. An individual decision for each measurement task seems indispensable. Especially for RC, the considerations are complex. Normal strength concrete cracks at a tensile strain of about 0.1 ‰. A temperature error of 5 °C would account for 50 % of this strain. However, scatter of the same size has hardly any influence on the measurement or testing of the yield strain of reinforcing steel (2.5 ‰).

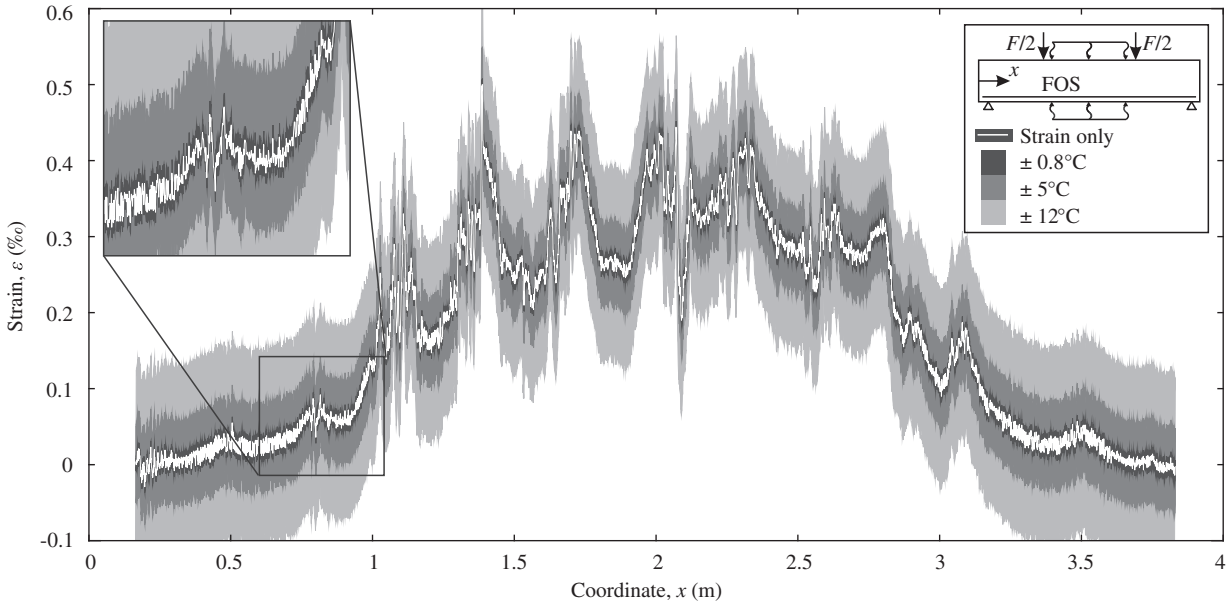

FIGURE 12 Reinforcement strains in the thermo-mechanical test along with scatter bands for residual temperatures of 0.8, 5, and 12 °C

TABLE 3 Comparison of deviations from unplanned temperature changes with characteristic strains (‰)

Strain error from temperature change			Measuring system		
0.8 °C	**5 °C**	**12 °C**	**Repeatability + accuracy**	**Strain at cracking of concrete**	**Strain at yielding of reinforcement**
0.008	0.05	0.12	0.047	0.1	2.5

5 | CONCLUSIONS

Rayleigh-based FOS measurements of RC structures promise fine-mesh data networks of substantial structural–mechanical quantities, that is, strain and temperature. Such pertains to both laboratory and real-life application scenarios. With interest in the coupling and corrupting interplay of temperature and mechanical strain measurements, consecutively executed tests were carried out on RC beams under mechanical, thermal, and thermo-mechanical loading, respectively. In addition to general quality and plausibility checks of the measured quantities, the investigations focused on the mutual influence of strain and temperature. Both the influence of parasitic strain on temperature measurement and that of temperature variance on mechanical strain measurement could be quantified. Produced findings are in line with the theoretical magnitude of the cross-effects deduced from simplification and mathematical conversion of fundamental equations of fiber optics.

In more detail, the following could be ascertained and contributed:

- Under laboratory conditions, strain can be recorded in an isolated, precise and quasi-continuous manner in place and time using FOS. The quality is sufficient to identify average component strains for deformation measurements and to track strain transfer during cracking in the composite region. Residual strains and resulting residual tensile forces at the support are obtained within normatively justified limits and consistent with established model concepts.
- It was demonstrated how the conversion of FOS-produced measurements may be calibrated more precisely with the assistance of TC, so as to obtain high-resolution temperature measurements across structures.
- In temperature measurement, the significant corrupting influence of involuntary strain effects, for example, from friction or contact, were emphasized. In absolute terms, the ratio of the conversion factors of temperature causes larger errors in strain measurement than the other way around (guesstimate: 1 °C leads to strain deviations of 10 µstrain or 1 µstrain to 0.1 °C temperature deviation). This must be put into

perspective for applications in practical construction since strain conventionally ranges between 100 to 1000 μstrain, whereas temperature changes only account for few degrees Celsius.

- Even with capillary installation of FOS intended to isolate the temperature effect, parasitic strains of significant magnitude can occur. Even strain corresponding to a force of only 0.05 N (5 g weight force) produces temperature measurement adulterations of about 6 °C. This must be considered a key explanation as to why temperature is rarely measured employing Rayleigh-based fiber optic systems, as opposed to strain measurement contexts.
- Strain measurement in real-world scenarios must account for the corrupting influence of temperature. A temperature change of 5 °C (diurnal cycle winter) already reaches the order of magnitude of the general measurement accuracy of the fiber optic system. If the system accuracy and the temperature-related variance of 5 °C add up, cracking can no longer be detected reliably—entailing consequential implications for construction monitoring purposes. Since both temperature variance and system accuracy remain invariable across testing scenarios, their corrupting impact on the respective measurement scenario decreases in relative terms, with increasing strain levels.
- With respect to the highly complex material behavior of RC, the permissible error size must always be checked for the specific measurement context.

ACKNOWLEDGMENTS

Financial support for this work was provided by Deutsche Forschungsgemeinschaft (DFG, German Research Foundation)—Project number 398216472. This support is gratefully acknowledged.

DATA AVAILABILITY STATEMENT

The data that support the findings of this study are available from the corresponding author upon reasonable request.

ORCID

Felix Clauß https://orcid.org/0000-0001-5361-3255
Mark Alexander Ahrens https://orcid.org/0000-0002-2337-1571
Peter Mark https://orcid.org/0000-0003-1812-2148

REFERENCES

1. Sanio D, Ahrens MA, Mark P, Rode S. Increasing the accuracy of lifetime prediction by structuralmonitoring of a 50-year old pre-stressed concrete bridge. Beton- Stahlbetonbau. 2014; 109(2):128–37. https://doi.org/10.1002/best.201300079
2. Müller A, Sodeikat C, Schänzlin J, Knab F, Albrecht L, Groschup R, et al. The Gänstor Bridge in Ulm—inspection, structural reanalysis, load test and bridge monitoring. Beton- Stahlbetonbau. 2020;115(3): 164–78. https://doi.org/10.1002/best.201900071
3. Sanio D, Löschmann J, Mark P, Ahrens MA. Measurements vs. analytical methods to evaluate fatigue of tendons in concrete bridges. Bautechnik. 2018;95(2):99–110. https://doi.org/10.1002/bate.201700092
4. Schacht G, Käding M, Bolle G, Marx S. Concepts for the assessment of bridges with the risk of stress corrosion cracking. Beton- Stahlbetonbau. 2018;114(2):85–94. https://doi.org/10.1002/best.201800087
5. Wang X, Niederleithinger E, Hindersmann I. The installation of embedded ultrasonic transducers inside a bridge to monitor temperature and load influence using coda wave interferometry technique. Struct Health Monit. 2022;21(3):913–27. https://doi.org/10.1177/14759217211014430
6. Bado MF, Casas JR. A review of recent distributed optical fiber sensors applications for civil engineering structural health monitoring. Sensors (Basel). 2021;21(5):1818. https://doi.org/10.3390/s21051818
7. Regier R, Hoult NA. Distributed strain behavior of a reinforced concrete bridge: case study. J Bridge Eng. 2014;19(12): 05014007. https://doi.org/10.1061/(ASCE)BE.1943-5592.0000637
8. Barrias A, Rodriguez G, Casas JR, Villalba S. Application of distributed optical fiber sensors for the health monitoring of two real structures in Barcelona. Struct Infrastruct Eng. 2018;14(7): 967–85. https://doi.org/10.1080/15732479.2018.1438479
9. Froggatt M, Moore J. High-spatial-resolution distributed strain measurement in optical fiber with rayleigh scatter. Appl Optics. 1998;37(10):1735–40. https://doi.org/10.1364/AO.37.001735
10. Gifford DK, Soller BJ, Wolfe MS, Froggatt ME. Distributed fiber-optic temperature sensing using Rayleigh backscatter. 31st European conference on optical communications (ECOC 2005). Glasgow: IEE; 2005.
11. Soller B, Gifford D, Wolfe M, Froggatt M. High resolution optical frequency domain reflectometry for characterization of components and assemblies. Opt Express. 2005;13(2):666–74. https://doi.org/10.1364/OPEX.13.000666
12. POLYTEC GmbH. Luna ODiSI 6000: optical distributed sensor interrogators (Data sheet).
13. Samiec D. Verteilte faseroptische Temperatur- und Dehnungsmessung mit sehr hoher Ortsauflösung. Fellbach, Germany: Photonik; 2011.
14. Novák B, Stein F, Reinhard J, Dudonu A. Surface application of distributed fiber optic sensors for bridge monitoring. Beton-Stahlbetonbau. 2021;116(10):718–26. https://doi.org/10.1002/best.202100070
15. Fischer O, Thoma S, Crepaz S. Distributed fiber optic sensing for crack detection in concrete structures. Civ Eng Design. 2019;1(3–4):97–105. https://doi.org/10.1002/cend.201900008
16. Konertz D, Kocur GK, Häusler F, Mark P. Longitudinal shear transmission of anchor channels into concrete—an experimental approach. Struct Concrete. 2021;22(2):1072–84. https://doi.org/10.1002/suco.202000133
17. Vogdt FD, Speck K, Petryna Y, Curbach M, Loutfi J. New experimental insights on concrete plasticity under triaxial

loading. Beton- Stahlbetonbau. 2021;82(15):1201. https://doi.org/10.1002/best.202100074
18. Grabke S, Clauß F, Bletzinger K-U, Ahrens MA, Mark P, Wüchner R. Damage detection at a reinforced concrete specimen with coda wave interferometry. Materials (Basel). 2021;14(17):5013. https://doi.org/10.3390/ma14175013
19. Kindler A, Großwig S. Distributed strain sensing in geotechnical—a first standard for fiber optic strain measurements in geotechnical engineering. Bautechnik. 2018;95(5):385–93. https://doi.org/10.1002/bate.201800005
20. Schenato L. A review of distributed fibre optic sensors for geo-hydrological applications. Appl Sci. 2017;7(9):896. https://doi.org/10.3390/app7090896
21. Monsberger CM, Lienhart W. Distributed fiber optic shape sensing along shotcrete tunnel linings: methodology, field applications, and monitoring results. J Civ Struct Health Monit. 2021;11(2):337–50. https://doi.org/10.1007/s13349-020-00455-8
22. Stegehake C, Grünewald M, Zanthoff H-W, Hecht C. Fiber-optic temperature measurements in fixed-bed reactors for model-based evaluation of effective radial thermal conductivity. Chem Ing Tech. 2018;90(5):602–14. https://doi.org/10.1002/cite.201700158
23. Ouyang J, Chen X, Huangfu Z, Lu C, Huang D, Li Y. Application of distributed temperature sensing for cracking control of mass concrete. Construct Build Mater. 2019;197(5):778–91. https://doi.org/10.1016/j.conbuildmat.2018.11.221
24. Löschmann J, Clauß F, Mark P. Strengthening of reinforced concrete structures with temperature induction. Beton- Stahlbetonbau. 2020;115(10):746–57. https://doi.org/10.1002/best.202000038
25. Löschmann J, Stolzuoli N, Ahrens MA, Mark P. Steering of continuity stresses in beam structures by temperature induction. Eng Struct. 2021;229(6):111621. https://doi.org/10.1016/j.engstruct.2020.111621
26. Hill KO, Meltz G. Fiber Bragg grating technology fundamentals and overview. J Lightwave Technol. 1997;15(8):1263–76. https://doi.org/10.1109/50.618320
27. Kersey AD, Davis MA, Patrick HJ, LeBlanc M, Koo KP, Askins CG, et al. Fiber grating sensors. J Lightwave Technol. 1997;15(8):1442–63. https://doi.org/10.1109/50.618377
28. Liehr S. Fibre optic sensing techniques based on incoherent optical frequency domain reflectometry [PhD thesis]. Berlin: Technischen Universität Berlin; 2014. Available from: http://www.bam.de/de/service/publikationen/publikationen_medien/dissertationen/diss125_vt.pdf
29. Künzel A. Parameteridentifikation auf Basis faseroptisch gemessener quasi-kontinuierlicher Dehnungssignale [PhD thesis]. Berlin: Technische Universität Berlin; 2016.
30. Measures RM. Structural monitoring with fiber optic technology. 1st ed. San Diego, CA: Elsevier Professional; 2001.
31. Ansari F. Practical implementation of optical fiber sensors in civil structural health monitoring. J Intell Mater Syst Struct. 2007;18(8):879–89. https://doi.org/10.1177/1045389X06075760
32. Engelbrecht R. B6.1—fiber optic strain and temperature sensing: overview of principles. Proceedings sensor 2017. Wunstorf: AMA Service GmbH; 2017. p. 255–60.
33. Engelbrecht R. Nichtlineare Faseroptik. Berlin, Heidelberg: Springer Berlin Heidelberg; 2014.
34. Luna Innovations Incorporated. Distributed fiber optic sensing: temperature coefficient for polyimide coated low bend loss fiber, in the 10°C–80°C range. 2014 [cited 2021 Oct 28]. Available from: https://lunainc.com/sites/default/files/assets/files/resource-library/LT_TD_EN-FY1405_TempCoeff_10to80.pdf
35. Luna Innovations Incorporated. Distributed fiber optic sensing: temperature coefficient for polyimide coated low bend loss fiber, in the −40°C to 200°C range; 2014 [cited 2021 Oct 28]. Available from: https://lunainc.com/sites/default/files/assets/files/resource-library/LT_TD_EN-FY1403_TempCoeff_-40to200.pdf
36. Kreger ST, Gifford DK, Froggatt ME, Soller BJ, Wolfe MS. High resolution distributed strain or temperature measurements in single- and multi-mode fiber using swept-wavelength interferometry. Optical fiber sensors. Washington, DC: OSA; 2006. p. ThE42.
37. Froggatt ME, Gifford DK, Kreger ST, Wolfe MS, Soller BJ. Distributed strain and temperature discrimination in unaltered polarization maintaining fiber. Optical fiber sensors. Washington, DC: OSA; 2006. p. ThC5.
38. ISOHEAT GmbH. Instruction manual ISOHEAT MIL-SM with temperature controller MIL-EC 550-PT.
39. Clauß F, Löschmann J, Ahrens MA, Mark P. Temperature induction into RC structures. Beton- Stahlbetonbau. 2021;116(7):539–50. https://doi.org/10.1002/best.202100010
40. Imai M, Feng M. Sensing optical fiber installation study for crack identification using a stimulated Brillouin-based strain sensor. Struct Health Monitor. 2012;11(5):501–9. https://doi.org/10.1177/1475921712442440
41. Duck G, LeBlanc M. Arbitrary strain transfer from a host to an embedded fiber-optic sensor. Smart Mater Struct. 2000;9(4):492–7. https://doi.org/10.1088/0964-1726/9/4/312
42. Bassil A, Chapeleau X, Leduc D, Abraham O. Concrete crack monitoring using a novel strain transfer model for distributed fiber optics sensors. Sensors (Basel). 2020;20(8):2220. https://doi.org/10.3390/s20082220
43. Konertz D, Löschmann J, Clauß F, Mark P. Fiber optic sensing of strain and temperature fields. Bauingenieur. 2019;94(7–8):292–300. https://doi.org/10.37544/0005-6650-2019-07-08-70
44. Clauß F, Epple N, Ahrens MA, Niederleithinger E, Mark P. Comparison of experimentally determined two-dimensional strain fields and mapped ultrasonic data processed by coda wave interferometry. Sensors (Basel). 2020;20(14):4023. https://doi.org/10.3390/s20144023
45. Clauß F, Ahrens MA, Mark P. A comparative evaluation of strain measurement techniques in reinforced concrete structures–a discussion of assembly, application, and accuracy. Struct Concr. 2021;22(5):2992–3007. https://doi.org/10.1002/suco.202000706
46. König G, Tue NV. Grundlagen und Bemessungshilfen für die Rißbreitenbeschränkung im Stahlbeton und Spannbeton sowie Kommentare, Hintergrundinformationen und Anwendungsbeispiele zu den Regelungen nach DIN 1045, EC2 und Model Code 90. Berlin: Beuth; 1996.
47. Zilch K, Zehetmaier G. Bemessung im konstruktiven Betonbau. Berlin, Heidelberg: Springer Berlin Heidelberg; 2010.
48. Feenstra PH, Borst R d. Constitutive model for reinforced concrete. J Eng Mech. 1995;121(5):587–95. https://doi.org/10.1061/(ASCE)0733-9399(1995)121:5(587)

49. Clauß F, Epple N, Ahrens MA, Niederleithinger E, Mark P. Correlation of load-bearing behavior of reinforced concrete members and velocity changes of coda waves. Materials (Basel). 2022;15(3):738. https://doi.org/10.3390/ma15030738
50. Davis MB, Hoult NA, Bajaj S, Bentz EC. Distributed sensing for shrinkage and tension stiffening measurement. ACI Struct J. 2017;114(3):753–64. https://doi.org/10.14359/51689463
51. Deutsches Institut für Normung e.V. DIN EN 1992-1-1: 2011–01, Eurocode_2: Bemessung und Konstruktion von Stahlbeton- und Spannbetontragwerken_- Teil_1–1: Allgemeine Bemessungsregeln und Regeln für den Hochbau; Deutsche Fassung EN_1992-1-1:2004_+ AC:2010. Berlin: Beuth Verlag GmbH; 2011.
52. Myers RH, Montgomery DC. Response surface methodology: process and product optimization using designed experiments. New York: Wiley; 1995.
53. Bassil A. Distributed fiber optics sensing for crack monitoring of concrete structures [PhD thesis]. Nantes: University of Nantes; 2019.

AUTHOR BIOGRAPHIES

Felix Clauß is at the Institute of Concrete Structures, Faculty of Civil and Environmental Engineering, Ruhr University Bochum, Germany. Email: felix.clauss@rub.de.

Mark Alexander Ahrens is at the Institute of Concrete Structures, Faculty of Civil and Environmental Engineering, Ruhr University Bochum, Germany. Email: alexander.ahrens@rub.de.

Peter Mark is at the Institute of Concrete Structures, Faculty of Civil and Environmental Engineering, Ruhr University Bochum, Germany. Email: peter.mark@rub.de.

How to cite this article: Clauß F, Ahrens MA, Mark P. Thermo-mechanical experiments on reinforced concrete beams: Assessing thermal, mechanical, and mixed impacts on fiber optic measurements. Structural Concrete. 2022. https://doi.org/10.1002/suco.202100890